

Colloidal Synthesis of Nanohelices via Bilayer Lattice Misfit

Yang Liu, Yuda Li, Soojin Jeong, Yi Wang, Jun Chen, and Xingchen Ye*



Cite This: *J. Am. Chem. Soc.* 2020, 142, 12777–12783



Read Online

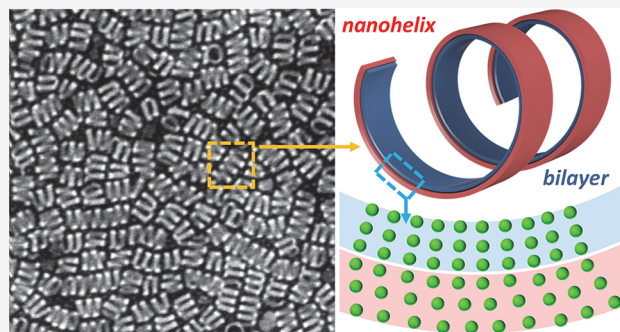
ACCESS |

Metrics & More

Article Recommendations

Supporting Information

ABSTRACT: Helical structures are ubiquitous in natural and synthetic materials across multiple length scales. Excellent and sometimes unusual chiral optical, mechanical, and sensing properties have been previously demonstrated in such symmetry-breaking shape, yet a general principle to realize helical structures at the sub-100 nm scale via colloidal synthesis remains underexplored. In this work, we describe the wet-chemical synthesis of monodisperse nanohelices based on gadolinium oxide (Gd_2O_3). Aberration-corrected electron microscopy revealed that individual nanohelices consist of a bilayer structure with the outer and inner layers derived from the $\{111\}$ and $\{100\}$ planes of bulk Gd_2O_3 , respectively. Distinct from existing inorganic nanocoils with flexible bending geometries, the built-in lattice misfit between two adjacent crystal planes induces continuous helical growth yielding three-dimensional rigid nanohelices. Furthermore, the presence of water in the reaction was found to suppress the formation of nanohelices, producing nanoplates expressing predominantly $\{111\}$ planes. Our study not only provides a bottom-up synthetic route and mechanistic understanding of nanohelices formation but may also open up new possibilities for creating chiral plasmonic nanostructures, luminescent biological labels, and nanoscale transducers.



INTRODUCTION

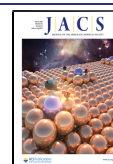
Helical structures that have fascinated scientists for centuries commonly exist in natural materials spanning multiple length scales. Examples include DNA molecules, plant tendrils, and seedpods.^{1,2} Over the past decades, synthetic helical and spiral structures have demonstrated their potential in a variety of applications ranging from sensing and actuation to micro-robotics, drug delivery, and optoelectronics.^{3–8} Sophisticated strain engineering techniques have been developed to create microscale and nanoscale helices using a large set of inorganic and organic materials such as lattice-mismatched semiconductor bilayers, prestressed membranes, hydrogels, and so on.^{9–13} The characteristic dimension of helical structures fabricated through a state-of-the-art strain engineering approach usually exceeds 100 nm, which is limited mainly by the resolution of top-down lithographic methods.^{9,14,15} The growth of helical structures has also been demonstrated in vapor-phase synthesis driven by electrostatic energy minimization or screw dislocation.^{4,16–18} Paralleling these advances there has been considerable development of solution-phase methods for the synthesis of colloidal nanocrystals in a rich variety of sizes and shapes.^{19–27} Notably, the interaction anisotropy between nanocrystal building blocks induced by external stimuli has been harnessed to construct helical superstructures via self-assembly.^{28,29} In recent years, colloidal two-dimensional (2D) colloidal nanocoils with flexible bending geometries and three-dimensional (3D) nanotubes have been realized in several materials systems including gadolinium

oxide, indium sulfide, and chalcogenide misfit compounds.^{30–34} However, one-step colloidal synthesis of 3D rigid nanohelices with high yield has not yet been reported.

Here, we report the solution-phase synthesis of highly uniform gadolinium oxide-based nanohelices. Aberration-corrected transmission electron microscopy (TEM) imaging revealed that individual nanohelices are composed of bilayer structures derived from the $\{100\}$ and $\{111\}$ planes of cubic-phase Gd_2O_3 . The continuum elasticity theory of strained bilayers is invoked to account for the resulting diameter of nanohelices, which highlights the crucial role of lattice misfit in driving continuous helical growth. By carefully drying the reaction precursors and conducting control experiments with small amounts of water intentionally added to the reaction, we elucidate the vital role of water in dictating the crystal habits of gadolinium Gd_2O_3 nanocrystals. Furthermore, we demonstrate that these nanohelices can be assembled into extended 2D and 3D superstructures exhibiting high positional and orientational order.

Received: May 11, 2020

Published: June 19, 2020



EXPERIMENTAL SECTION

Chemicals. Gadolinium(III) 2,4-pentanedionate hydrate, ($\text{Gd}(\text{acac})_3$, 99.9%), and anhydrous lithium hydroxide (LiOH , 98%) were purchased from Alfa Aesar. Oleic acid (OA, 90%), 1-octadecene (ODE, 90%), oleylamine (OAm, 70%), and ethylene glycol (EG, ≥99%) were purchased from Sigma-Aldrich. Several reagents were dried under vacuum (below 0.06 Torr) at elevated temperatures (110 °C for OA, 100 °C for OAm, and 95 °C for ODE) for at least 4 h and stored in a nitrogen-filled glovebox for future use. Other chemicals were used as received without further purification.

Synthesis of Gd_2O_3 Nanohelices. All syntheses were performed by using standard Schlenk line techniques under nitrogen atmosphere. In a typical reaction, 0.75 mmol of $\text{Gd}(\text{acac})_3$, 2 mmol of LiOH , 1 mL of OA, 4.5 mL of OAm, and 7.5 mL of ODE were loaded into a 50 mL three-neck flask inside a nitrogen-filled glovebox. The flask was then removed from the glovebox and connected to a Schlenk line in a fume hood. The reaction mixture was heated with a 3 °C/min ramp to 110 °C and kept at this temperature under vacuum (below 0.1 Torr) for 8 h. After refilling with nitrogen, the reaction mixture was heated at a ramp of 18 °C/min to 290 °C. The reaction was allowed to proceed at 290 °C for 1 h before being air-cooled to room temperature. The nanocrystal products were isolated by ethanol precipitation and centrifugation at 4000 rpm for 2 min. The precipitates were redispersed in 10 mL of toluene, and 7.5 mL of ethanol was added. A second round of centrifugation was carried out at 4000 rpm for 2 min to remove excess ligands and impurities such as lithium oleate (LiOL). The nanocrystals were finally dispersed in 20 mL of toluene.

Purification of Gd_2O_3 Nanohelices. Crude reaction products often include minor fractions of square and triangular/tripodal nanoplates. To separate nanohelices from other shape impurities, crude nanocrystal products dissolved in 20 mL of toluene were centrifuged at 2000 rpm for 2 min (i.e., without nonsolvent). Afterward, the pellet was mainly composed of nanoplates, and the supernatant solution enriched with nanohelices was carefully decanted into a glass vial for storage.

Self-Assembly of Nanohelices into Superlattices. Nanocrystal superlattices were formed by drying dispersed nanohelices on top of the immiscible EG liquid subphase.^{35,36} In a typical process, 10 μL of toluene solution (5 mg/mL) of nanohelices was drop-cast onto the surface of EG in a Teflon well ($1.5 \times 1.5 \times 1.5 \text{ cm}^3$). The well was subsequently covered with a glass slide to slow down solvent evaporation. After 4 h, the superlattice film was transferred onto a carbon-coated Cu TEM grid, which was further dried in a vacuum oven to remove residual EG.

Characterization. Low-magnification TEM images were acquired on a JEOL JEM 1400 plus microscope equipped with a LaB_6 filament operating at 120 kV. High-angle annular dark-field scanning TEM (HAADF-STEM) images and STEM energy-dispersive X-ray spectroscopy (STEM-EDS) maps were collected on a 300 kV JEOL JEM 3200FS TEM. Aberration-corrected STEM (AC-STEM) images and AC-STEM-EDX maps were recorded on a 200 kV JEOL JEM-ARM200F STEM equipped with spherical aberration correctors. Proton nuclear magnetic resonance ($^1\text{H NMR}$) measurements were performed on a Varian Inova 600 MHz spectrometer. NMR samples were prepared by mixing 20 μL of analyte with 600 μL of deuterated chloroform. The chemical shifts were referenced to the residual chloroform signal at 7.26 ppm.

RESULTS AND DISCUSSION

Gd_2O_3 nanohelices were synthesized via thermal decomposition of gadolinium acetylacetone precursor in mixed solvents of OA, OAm, and ODE at 290 °C for 1 h. Low-magnification TEM images reveal that as-synthesized nanohelices are highly uniform and appear rigid (Figure 1a and Figure S1), which is distinct from previously reported gadolinium oxide-based nanocoils or nanoscrolls exhibiting flexible bending geometries.^{30,32,37} Contrast variation at

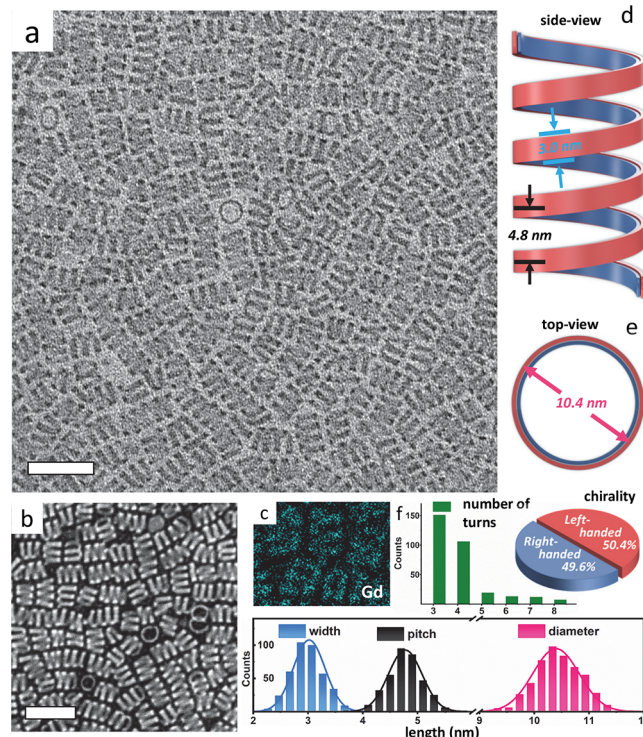


Figure 1. (a) Representative TEM image, (b) HAADF-STEM image, and (c) Gd elemental map of Gd_2O_3 nanohelices. (d) Schematic illustration of a single nanohelix: (d) side view; (e) top view. (f) Statistical analysis of morphological characteristics of nanohelices. The frequency distribution histograms are plotted for nanohelix width, pitch, diameter, number of turns, and helicity. Scale bars: 30 nm.

different positions of individual nanohelices as seen in the HAADF-STEM image further confirms the helical morphology (Figure 1b). STEM-EDS elemental mapping results indicate that gadolinium species are distributed homogeneously throughout the entire nanohelices (Figure 1c and Figure S2). The diameter d and width b of the helices are 10.4 ± 0.4 and 3.0 ± 0.3 nm, respectively (Figure 1d–f). The helical pitch p is measured to be 4.8 ± 0.4 nm (Figure 1d, f), resulting in a helical angle α of $\sim 8.4^\circ$ (Figure S3).¹⁴ The population ratio between left-handed and right-handed nanohelices is nearly 1:1 (156:154 from examination of 310 nanohelices as shown in Figure 1f), suggesting that there is no stereoselective preference during the formation of these nanohelices.

Aberration-corrected electron microscopy imaging was employed to probe the detailed atomic structure of individual nanohelices. Top-view AC-STEM images show that each nanohelix is composed of two distinct groups of lattice planes along its radial direction (Figure 2a and Figure S4). Moreover, the lattice planes of the inner layer appear to point toward the center of the helix, whereas those in the outer layer are tilted away from the radial direction by about 19° (Figure 2b). A visible gap of 1.2 Å separating the inner and outer layers was observed from the top view of a single-turn nanocoil (Figure 2a, c) or the perspective view of a multiturn nanohelix (Figure 2d). It should be noted that these single-turn nanocoils are not closed nanorings but rather underdeveloped helical structures, as manifested by the overlapping coil ends seen in the AC-HAADF-STEM image (Figure 2a). Notably, the side-view AC-STEM image of a single nanohelix reveals clear lattice

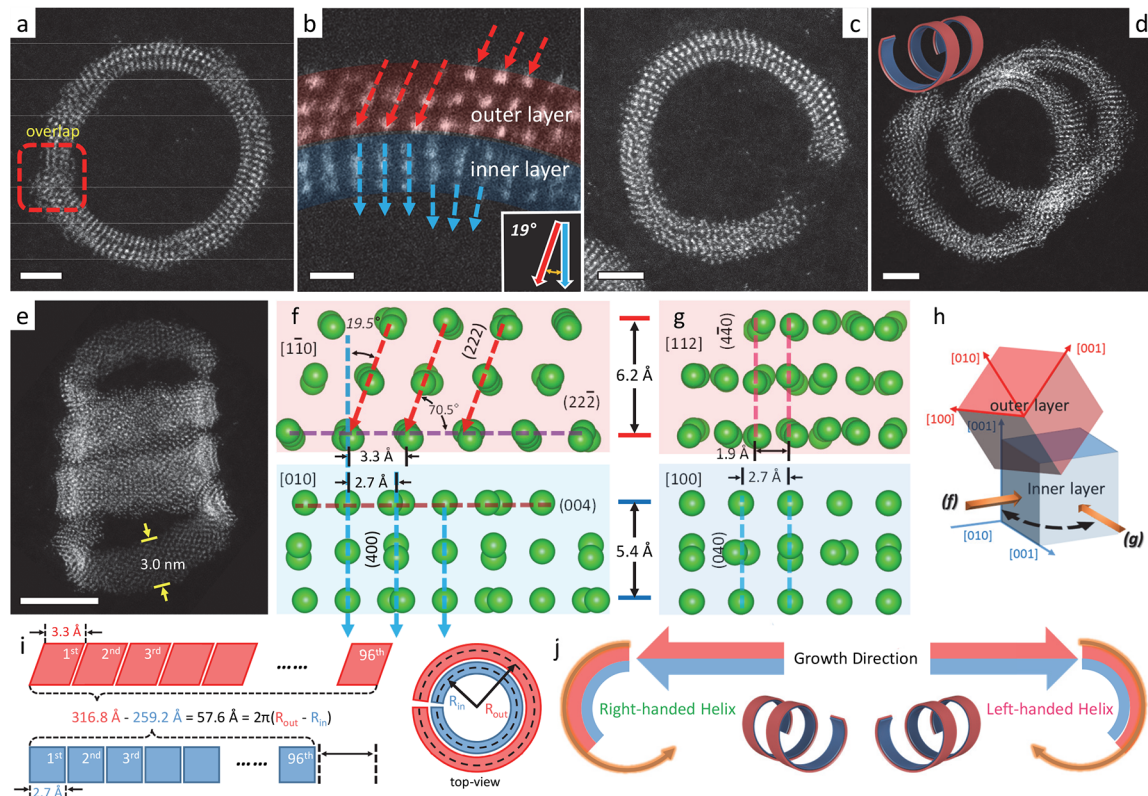


Figure 2. (a) Representative top-view AC-HAADF-STEM image of a single-turn nanohelix. The red-dashed box highlights vertically offset ends that appear to be partially overlapping when viewed along the helical axis. (b) AC-HAADF-STEM image showing a magnified view of the bilayer structure. The dashed arrows highlight the inner and outer layer crystal planes. (c–e) AC-HAADF-STEM images of (c) a single-turn nanocoil and (d, e) multturn nanohelices (d: perspective view; e: side view). (f–g) Crystal structure model for the radial bilayer of Gd_2O_3 nanohelices. The oxygen atoms have been omitted for clarity. (h) Schematic illustration of the relative orientation between the outer and inner layers. The zone axes in (f) and (g) are orthogonal to each other. (i–j) Illustration of (i) the lattice misfit between the {222}-bound outer layer and the {400}-bound inner layer and (j) growth directions of nanohelices. Scale bars: (a) 2 nm; (b) 5 Å; (c, d) 2 nm; (e) 5 nm.

structures when imaged along the radial direction (Figure 2e). This observation suggests that the outer and inner layers are likely made up of low-index crystal planes.

The interplanar spacings of the outer and inner layers are measured to be about 3.1 and 2.7 Å, respectively (indicated by dashed arrows in Figure 2b). These values are well matched to the interplanar distance of (222) and (400) crystal planes of cubic-phase Gd_2O_3 (space group: $Ia3$; lattice constant: 10.8 Å). An angle of 70.5° was measured between the (222) planes and the tangential direction in the outer layer, suggesting that the outer layer surface corresponds to the (222) plane of Gd_2O_3 (Figure 2b, f). On the other hand, the (400) planes of the inner layer are found to be perpendicular to the tangential direction, from which the inner layer surface can be indexed to the (004) plane of Gd_2O_3 (Figure 2b, f). Taken together, structural characterization of the bilayer at the subnanometer scale provides compelling evidence that individual nanohelices consist of a symmetry-breaking bilayer structure along their thickness (or radial) direction. The outer layer is oriented with the [1-10] direction along the helical axis and its surface derived from {222} planes, whereas the inner layer is aligned with the [010] direction along the helical axis and its surface stabilized with {400} planes (Figure 2f–h and Figures S5–S7).

The crude reaction products of current synthesis often contain small fractions of impurity shapes (below 30% in terms of particle number percentage), notably tripodal and square nanoplates (Figure 3a). AC-HAADF-STEM imaging reveals

that the tripodal plates are bounded by {111}-type crystal planes while the basal planes of square plates are the {100}-type (Figure 3b–e). These structural results are consistent with examples of different rare-earth oxide nanoplates previously reported by other researchers.^{38–42} Importantly, they also indicate that nanohelices likely form under conditions whereby both {111}- and {100}-type surface facets are favored. Previous works on colloidal Gd_2O_3 nanoparticles have shown that lithium oleate (LiOL) may promote the growth of {111}-terminated nanoplates.^{30,42} Moreover, density functional theory (DFT) calculations indicated that water molecules coordinate preferentially with the cation-rich {100} planes of Gd_2O_3 .⁴⁰

To unravel the potentially vital roles of water in the crystal habit control of Gd_2O_3 nanocrystals, we performed a series of experiments while controlling the amount of water present in the reaction. Vacuum degassing at 90–120 °C has been used routinely in colloidal nanocrystal synthesis to remove oxygen and moisture and to increase reproducibility and sample quality, although a short evacuation time (less than 1 h) could lead to incomplete removal of water especially when the liquid reagents are not predried or the reaction mixture is slowly producing water. Experimentally it was found that the synthesis of Gd_2O_3 nanohelices becomes highly reproducible when the liquid reagents (i.e., OA, OAm, and ODE) are predried and the reaction mixture is subjected to prolonged evacuation at 110 °C. In contrast, the nanohelices were barely formed when

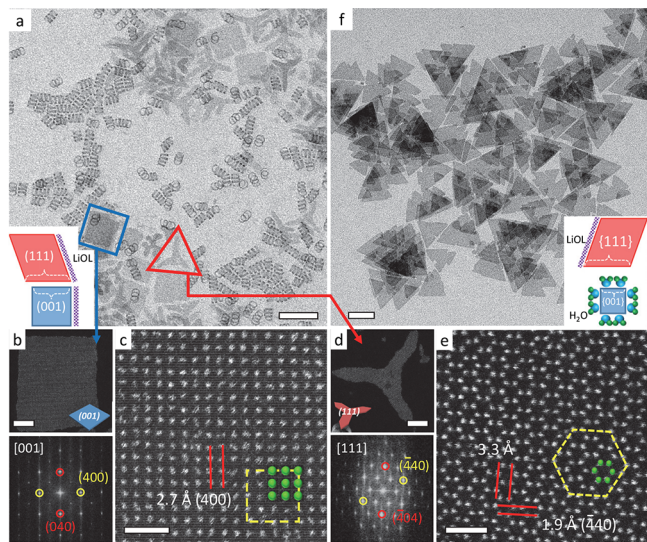


Figure 3. (a, f) Representative TEM images of crude reaction products synthesized (a) under typical reaction conditions for nanohelices and (f) with intentionally added water at the level of 2.3% (v/v). Insets: Scheme showing the impact of water on the crystal growth habits of Gd_2O_3 . (b–e) AC-HAADF-STEM images and corresponding fast Fourier transform (FFT) patterns of reaction byproducts, namely, (b–c) square and (d–e) tripodal nanoplates highlighted in (a). Scale bars: (a) 50, (b) 5, (c) 1, (d) 5, (e) 1, and (f) 50 nm.

a shorter evacuation time was employed (Figure S8a). The NMR spectrum of predried liquid reagents shows no change in its chemical structure (Figure S9). These results show that water may have a deleterious impact on the formation of nanohelices. Next, we carried out syntheses by drying the reaction mixture and then deliberately adding controlled amounts of water back to the reaction. When water was introduced at the level of 0.08% (v/v), the formation of nanohelices was significantly suppressed, and reaction products were mostly irregularly shaped nanoplates (Figure S8b). As more water was added, a higher fraction of {111}-bound triangular nanoplates resulted with a concomitant decrease in {100}-bound nanoplates. At the level of 2.31% (v/v) of added water, well-faceted triangular nanoplates were found to be the major product (Figure 3f). Collectively, these results demonstrate that a trace amount of water is sufficient to suppress the growth of {100} planes of Gd_2O_3 , which is in line with insights from DFT calculations.⁴⁰

Based on the structural model shown in Figure 2f, it is conceivable that the formation of Gd_2O_3 nanohelices would require a delicate balance between the growth rate of {111} and {100} crystal planes. In fact, both the ramp rate and the reaction temperature have a drastic influence on the reaction outcome. The yield of nanohelices became vanishingly small when the reaction ramp rate was set to be 10 °C/min or less (Figure S11). On the other hand, single- and half-turn nanohelices were found to be the major products when the ramp rate exceeded 25 °C/min (Figure S11). Furthermore, the high yield of nanohelices was maintained when lowering the reaction temperature from 290 to 270 °C, whereas {100}-bound nanoplates predominated when the reaction was run at 310 °C (Figure S11).

We now discuss the physical mechanism underlying the formation of Gd_2O_3 nanohelices. The lattice misfit (2.7 vs 3.3

Å, $\epsilon = 18\%$) induces elastic strains within the bilayer structure. Considering that the entire bilayer is only 1.3 ± 0.1 nm thick, there is a strong tendency for the compressively strained outer layer and the tensile-strained inner layer to bend such that the misfit strain could be partially relaxed. The growth and bending of the ribbonlike bilayer can take place concurrently so that relaxation of misfit strain occurs as it builds up along the helical growth path (Movie S1). This mechanistic picture is reinforced further by the fact that nanocoils formed at shorter reaction times share the same bilayer structure as those multturn nanohelices (Figure 2c and Figure S10). The difference in perimeter between the inner and outer layers measured from dozens of nanohelices turns out to be about 57.6 Å. This translates into 96 atomic planes around the circumference of each nanohelix based on the lattice misfit of 0.6 Å (Figure 2i) and matches well with the value retrieved from direct counting in the AC-HAADF-STEM images (Figure S4). Further, the misfit strain within the bilayer establishes a preferred bending direction, and therefore the formation of spaghetti-like random nanocoils is strongly disfavored (Figure 2j). Indeed, we did not observe any coexisting flexible nanocoils in our nanohelix samples. This finding is in stark contrast with previous reports of self-adjustable gadolinium oxide and indium sulfide nanocoils.^{30–32}

For a strained bilayer, its bending diameter is principally determined by the layer thickness and lattice mismatch due to the interplay between stretching and bending energies. Upon bending of a bilayer structure, the stretching energy associated with lattice misfit is lowered at the expense of increasing bending energy. Considering that stretching energy scales linearly with layer thickness while bending energy scales with the cube of its thickness, it is anticipated that thinner strained bilayers have greater tendency to curve compared to thicker ones. In order to predict the diameter of the helix resulting from a strained bilayer, the following equation derived from continuum elasticity theory can be used:

$$D_{\text{helix}}^{\text{inner}} = \frac{d_{\text{in}}^4 + 4\chi d_{\text{in}}^3 d_{\text{out}} + 6\chi d_{\text{in}}^2 d_{\text{out}}^2 + 4\chi d_{\text{in}} d_{\text{out}}^3 + d_{\text{out}}^4 \chi^2}{3\epsilon\chi(1+\nu)d_{\text{in}} d_{\text{out}}(d_{\text{in}} + d_{\text{out}})} \quad (1)$$

where d_{in} and d_{out} are the inner and outer layer thickness, ϵ is the lattice misfit, χ is Young's modulus ratio between two layers, and ν is Poisson's ratio.^{14,43,44} To quantitatively assess the role of misfit strain in directing the formation of Gd_2O_3 nanohelices, we calculate the helix inner diameter using eq 1. As detailed in Table S1, theoretical $D_{\text{helix}}^{\text{inner}}$ values fall in the range of 6.9–7.6 nm, which is in good agreement with the 7.5 ± 0.4 nm inner diameter of Gd_2O_3 nanohelices measured from HAADF-STEM images.

The narrow range of nanohelix diameters predicted by continuum elasticity theory further indicates that the formation of planar multturn Gd_2O_3 spirals is energetically highly unfavorable. Considering a hypothetical 2D multturn nano-spiral built on the same Gd_2O_3 bilayer, the diameter of the second turn would have increased by nearly 6 nm (sum of twice the bilayer thickness and alkyl ligand lengths), which far exceeds the optimal diameters for strain relaxation. Indeed, we observed that nanocoils having a contour length slightly larger than that required to complete one full turn exhibit a clear tendency to continue growing into 3D nanohelices rather than 2D nanospirals (Figure 2a and Figure S4). The width of the bilayer is another important parameter that controls the

formation of the helical structure. The minimum helical angle is set by the ratio between the width of the bilayer (3.0 ± 0.3 nm) and the average outer perimeter of the helix (32.7 nm) and is calculated to be 5.2° by using the formula $\theta = \tan^{-1}\left(\frac{W}{\pi D_{\text{outer}}}\right)$. This value is slightly smaller than the experimentally determined helical angle of 8.4° for Gd_2O_3 nanohelices (Figure S3).¹⁴

Monodisperse colloidal nanohelices represent a new family of nanocrystal building blocks that can be assembled into long-range-ordered superstructures with prescribed lattice symmetries.³⁶ Parts a and b in Figure 4 shows TEM and HAADF-

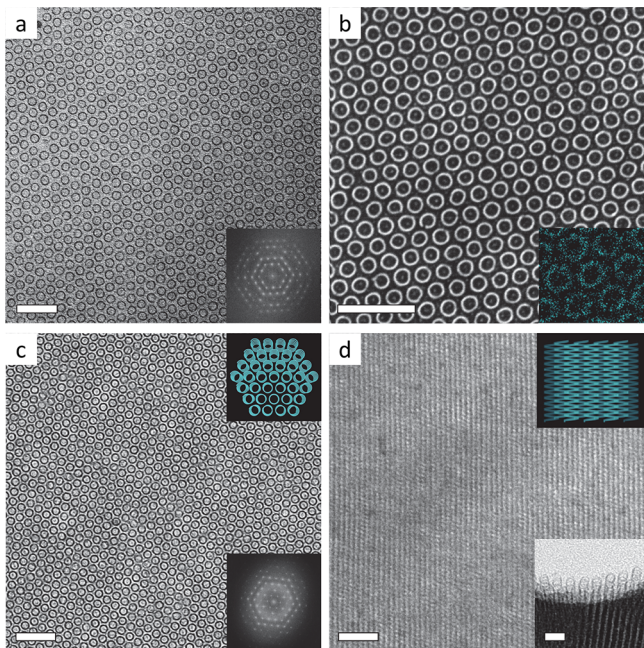


Figure 4. (a) TEM and (b) HAADF-STEM images of 2D hexagonal superlattices self-assembled from single-turn nanohelices. (c, d) TEM images of superlattices self-assembled from multturn nanohelices at different particle solution concentrations. The bottom insets of (a) and (c) show the corresponding FFT patterns. Inset of (b): Gd elemental map. The upper right insets of (c) and (d) show the structural model of superlattices. The bottom inset of (d) shows a TEM image acquired near the edge of the superlattices. Scale bars: (a–d) 50 nm; inset of (d) 20 nm.

STEM images of 2D hexagonal superlattices of single-turn nanohelices. The average distance between nearest-neighbor nanohelices was measured to be 2.3 ± 0.2 nm, which indicates the presence of alkyl ligands. Moreover, the bending diameters of individual nanohelices in the closed-packed array remain essentially unchanged, further confirming their structural rigidity. Notably, superlattices assembled from multturn nanohelices exhibit preferred orientations depending on the particle solution concentration. At relatively low concentrations (5 mg/mL), a 2D hexagonal lattice comprised of vertically standing nanohelices was obtained (Figure 4c and Figure S12). At higher concentrations (10 mg/mL), dense multilayers form with individual nanohelices aligned horizontally (Figure 4d). The periodic striplike contrast is believed to arise from superimposed rims of adjacent nanohelices (Figure 4c and Figure S13).

CONCLUSION

In conclusion, we have developed a new synthetic route for monodisperse colloidal Gd_2O_3 nanohelices. Aberration-corrected electron microscopy imaging indicates that individual nanohelices are characterized as a bilayer structure with the outer and inner layers derived from the {111} and {100} planes of cubic-phase Gd_2O_3 , respectively. The built-in lattice misfit between the two layers drives helical crystal growth at elevated temperatures producing 3D rigid nanohelices. Continuum elasticity theory of strained bilayers is found to accurately predict the diameter of nanohelices, which provides compelling evidence that lattice misfit plays a central role in the growth of nanohelices. We further elucidate the importance of water in controlling the crystal habits of gadolinium oxide and the formation of nanohelices. Altogether, our work introduces a new type of “exotic” nanocolloids and could open up further possibilities for understanding and controlling crystal growth with subnanometer precision.

ASSOCIATED CONTENT

Supporting Information

The Supporting Information is available free of charge at <https://pubs.acs.org/doi/10.1021/jacs.0c05175>.

Growth and bending of ribbonlike bilayer (MOV)

Additional TEM and STEM images of nanohelices; crystal structure models of cubic Gd_2O_3 ; NMR spectra of liquid reagents; nanocrystals synthesized under different conditions; additional TEM images of nano-helix superlattices (PDF)

AUTHOR INFORMATION

Corresponding Author

Xingchen Ye — Department of Chemistry, Indiana University, Bloomington, Indiana 47405, United States; orcid.org/0000-0001-6851-2721; Email: xingye@indiana.edu

Authors

Yang Liu — Department of Chemistry, Indiana University, Bloomington, Indiana 47405, United States

Yuda Li — Department of Chemistry, Indiana University, Bloomington, Indiana 47405, United States

Soojin Jeong — Department of Chemistry, Indiana University, Bloomington, Indiana 47405, United States

Yi Wang — Department of Chemistry, Indiana University, Bloomington, Indiana 47405, United States

Jun Chen — Department of Chemistry, Indiana University, Bloomington, Indiana 47405, United States

Complete contact information is available at: <https://pubs.acs.org/10.1021/jacs.0c05175>

Funding

The authors acknowledge financial support from Indiana University through the FRSP-Seed program and National Science Foundation under award number CHE-1808027.

Notes

The authors declare no competing financial interest.

ACKNOWLEDGMENTS

We thank the Indiana University Nanoscale Characterization Facility and Electron Microscopy Center for access of instrumentation.

■ REFERENCES

- (1) Gerbode, S. J.; Puzey, J. R.; McCormick, A. G.; Mahadevan, L. How the Cucumber Tendril Coils and Overwinds. *Science* **2012**, *337*, 1087–1091.
- (2) Armon, S.; Efrati, E.; Kupferman, R.; Sharon, E. Geometry and Mechanics in the Opening of Chiral Seed Pods. *Science* **2011**, *333*, 1726–1730.
- (3) Mokashi-Punekar, S.; Zhou, Y.; Brooks, S. C.; Rosi, N. L. Construction of Chiral, Helical Nanoparticle Superstructures: Progress and Prospects. *Adv. Mater.* **2019**, e1905975.
- (4) Ren, Z.; Gao, P. X. A Review of Helical Nanostructures: Growth Theories, Synthesis Strategies and Properties. *Nanoscale* **2014**, *6*, 9366–9400.
- (5) Chen, Z. Geometric Nonlinearity and Mechanical Anisotropy in Strained Helical Nanoribbons. *Nanoscale* **2014**, *6*, 9443–9447.
- (6) Wang, Y.; Xu, J.; Wang, Y.; Chen, H. Emerging Chirality in Nanoscience. *Chem. Soc. Rev.* **2013**, *42*, 2930–2962.
- (7) Ma, W.; Xu, L.; de Moura, A. F.; Wu, X.; Kuang, H.; Xu, C.; Kotov, N. A. Chiral Inorganic Nanostructures. *Chem. Rev.* **2017**, *117*, 8041–8093.
- (8) Wang, Y.; He, J.; Mu, X.; Wang, D.; Zhang, B.; Shen, Y.; Lin, M.; Kubel, C.; Huang, Y.; Chen, H. Solution Growth of Ultralong Gold Nanohelices. *ACS Nano* **2017**, *11*, 5538–5546.
- (9) Bell, D. J.; Dong, L.; Nelson, B. J.; Golling, M.; Zhang, L.; Grutzmacher, D. Fabrication and Characterization of Three-Dimensional InGaAs/GaAs Nanosprings. *Nano Lett.* **2006**, *6*, 725–729.
- (10) Prinz, V. Y.; Seleznev, V. A.; Gutakovskiy, A. K.; Chehovskiy, A. V.; Preobrazhenskii, V. V.; Putyato, M. A.; Gavrilova, T. A. Free-Standing and Overgrown InGaAs/GaAs Nanotubes, Nanohelices and Their Arrays. *Phys. E* **2000**, *6*, 828–831.
- (11) Mei, Y.; Huang, G.; Solovev, A. A.; Ureña, E. B.; Mönch, I.; Ding, F.; Reindl, T.; Fu, R. K. Y.; Chu, P. K.; Schmidt, O. G. Versatile Approach for Integrative and Functionalized Tubes by Strain Engineering of Nanomembranes on Polymers. *Adv. Mater.* **2008**, *20*, 4085–4090.
- (12) Wu, Z. L.; Moshe, M.; Greener, J.; Therien-Aubin, H.; Nie, Z.; Sharon, E.; Kumacheva, E. Three-Dimensional Shape Transformations of Hydrogel Sheets Induced by Small-Scale Modulation of Internal Stresses. *Nat. Commun.* **2013**, *4*, 1586.
- (13) Zhang, H.; Mourran, A.; Möller, M. Dynamic Switching of Helical Microgel Ribbons. *Nano Lett.* **2017**, *17*, 2010–2014.
- (14) Zhang, L.; Ruh, E.; Grutzmacher, D.; Dong, L.; Bell, D. J.; Nelson, B. J.; Schonenberger, C. Anomalous Coiling of SiGe/Si and SiGe/Si/Cr Helical Nanobelts. *Nano Lett.* **2006**, *6*, 1311–1317.
- (15) Huang, G.; Mei, Y. Helices in Micro-World: Materials, Properties, and Applications. *J. Materomics* **2015**, *1*, 296–306.
- (16) Liu, Y.; Wang, J.; Kim, S.; Sun, H.; Yang, F.; Fang, Z.; Tamura, N.; Zhang, R.; Song, X.; Wen, J.; Xu, B. Z.; Wang, M.; Lin, S.; Yu, Q.; Tom, K. B.; Deng, Y.; Turner, J.; Chan, E.; Jin, D.; Ritchie, R. O.; Minor, A. M.; Chirzan, D. C.; Scott, M. C.; Yao, J. Helical van der Waals Crystals With Discretized Eshelby Twist. *Nature* **2019**, *570*, 358–362.
- (17) Gao, P. X.; Ding, Y.; Mai, W.; Hughes, W. L.; Lao, C.; Wang, Z. L. Conversion of Zinc Oxide Nanobelts into Superlattice-Structured Nanohelices. *Science* **2005**, *309*, 1700–1704.
- (18) Bierman, M. J.; Lau, Y. K.; Kvit, A. V.; Schmitt, A. L.; Jin, S. Dislocation-Driven Nanowire Growth and Eshelby Twist. *Science* **2008**, *320*, 1060–1063.
- (19) Murphy, C. J.; Sau, T. K.; Gole, A. M.; Orendorff, C. J.; Gao, J.; Gou, L.; Hunyadi, S. E.; Li, T. Anisotropic Metal Nanoparticles: Synthesis, Assembly, and Optical Applications. *J. Phys. Chem. B* **2005**, *109*, 13857–13870.
- (20) Yin, Y.; Alivisatos, A. P. Colloidal Nanocrystal Synthesis and the Organic-Inorganic Interface. *Nature* **2005**, *437*, 664–670.
- (21) Park, J.; Joo, J.; Kwon, S. G.; Jang, Y.; Hyeon, T. Synthesis of Monodisperse Spherical Nanocrystals. *Angew. Chem., Int. Ed.* **2007**, *46*, 4630–4660.
- (22) Wang, F.; Han, Y.; Lim, C. S.; Lu, Y.; Wang, J.; Xu, J.; Chen, H.; Zhang, C.; Hong, M.; Liu, X. Simultaneous Phase and Size Control of Upconversion Nanocrystals Through Lanthanide Doping. *Nature* **2010**, *463*, 1061–1065.
- (23) Personick, M. L.; Mirkin, C. A. Making Sense of the Mayhem Behind Shape Control in the Synthesis of Gold Nanoparticles. *J. Am. Chem. Soc.* **2013**, *135*, 18238–18247.
- (24) Kovalenko, M. V.; Manna, L.; Cabot, A.; Hens, Z.; Talapin, D. V.; Kagan, C. R.; Klimov, V. I.; Rogach, A. L.; Reiss, P.; Milliron, D. J.; Guyot-Sionnest, P.; Konstantatos, G.; Parak, W. J.; Hyeon, T.; Korgel, B. A.; Murray, C. B.; Heiss, W. Prospects of Nanoscience with Nanocrystals. *ACS Nano* **2015**, *9*, 1012–1057.
- (25) Pang, X.; He, Y.; Jung, J.; Lin, Z. 1D Nanocrystals with Precisely Controlled Dimensions, Compositions, and Architectures. *Science* **2016**, *353*, 1268–1272.
- (26) Huo, D.; Kim, M. J.; Lyu, Z.; Shi, Y.; Wiley, B. J.; Xia, Y. One-Dimensional Metal Nanostructures: From Colloidal Syntheses to Applications. *Chem. Rev.* **2019**, *119*, 8972–9073.
- (27) Steimle, B. C.; Fenton, J. L.; Schaak, R. E. Rational Construction of a Scalable Heterostructured Nanorod Megalibrary. *Science* **2020**, *367*, 418–424.
- (28) Singh, G.; Chan, H.; Baskin, A.; Gelman, E.; Repnin, N.; Král, P.; Klajn, R. Self-Assembly of Magnetite Nanocubes into Helical Superstructures. *Science* **2014**, *345*, 1149–1153.
- (29) Srivastava, S.; Santos, A.; Critchley, K.; Kim, K. S.; Podsiadlo, P.; Sun, K.; Lee, J.; Xu, C.; Lilly, G. D.; Glotzer, S. C.; Kotov, N. A. Light-Controlled Self-Assembly of Semiconductor Nanoparticles into Twisted Ribbons. *Science* **2010**, *327*, 1355–1359.
- (30) Luo, D.; Cui, S.; Liu, Y.; Shi, C.; Song, Q.; Qin, X.; Zhang, T.; Xue, Z.; Wang, T. Biocompatibility of Magnetic Resonance Imaging Nanoprobes Improved by Transformable Gadolinium Oxide Nano-coils. *J. Am. Chem. Soc.* **2018**, *140*, 14211–14216.
- (31) Ni, B.; Liu, H.; Wang, P. P.; He, J.; Wang, X. General Synthesis of Inorganic Single-Walled Nanotubes. *Nat. Commun.* **2015**, *6*, 8756.
- (32) Wang, P. P.; Yang, Y.; Zhuang, J.; Wang, X. Self-Adjustable Crystalline Inorganic Nanocoils. *J. Am. Chem. Soc.* **2013**, *135*, 6834–6837.
- (33) Paek, J.; Lee, C. H.; Choi, J.; Choi, S. Y.; Kim, A.; Lee, J. W.; Lee, K. Gadolinium Oxide Nanoring and Nanoplate: Anisotropic Shape Control. *Cryst. Growth Des.* **2007**, *7*, 1378–1380.
- (34) Visic, B.; Panchakarla, L. S.; Tenne, R. Inorganic Nanotubes and Fullerene-like Nanoparticles at the Crossroads between Solid-State Chemistry and Nanotechnology. *J. Am. Chem. Soc.* **2017**, *139*, 12865–12878.
- (35) Dong, A.; Chen, J.; Vora, P. M.; Kikkawa, J. M.; Murray, C. B. Binary Nanocrystal Superlattice Membranes Self-Assembled at the Liquid-Air Interface. *Nature* **2010**, *466*, 474–477.
- (36) Ye, X.; Collins, J. E.; Kang, Y.; Chen, J.; Chen, D. T.; Yodh, A. G.; Murray, C. B. Morphologically Controlled Synthesis of Colloidal Upconversion Nanophosphors and Their Shape-Directed Self-Assembly. *Proc. Natl. Acad. Sci. U. S. A.* **2010**, *107*, 22430–22435.
- (37) Wu, M.; Xue, Y.; Li, N.; Zhao, H.; Lei, B.; Wang, M.; Wang, J.; Luo, M.; Zhang, C.; Du, Y.; Yan, C. Tumor-Microenvironment-Induced Degradation of Ultrathin Gadolinium Oxide Nanoscrolls for Magnetic-Resonance-Imaging-Monitored, Activatable Cancer Chemotherapy. *Angew. Chem., Int. Ed.* **2019**, *58*, 6880–6885.
- (38) Si, R.; Zhang, Y. W.; Zhou, H. P.; Sun, L. D.; Yan, C. H. Controlled-Synthesis, Self-Assembly Behavior, and Surface-Dependent Optical Properties of High-Quality Rare-Earth Oxide Nanocrystals. *Chem. Mater.* **2007**, *19*, 18–27.
- (39) Si, R.; Zhang, Y. W.; You, L. P.; Yan, C. H. Rare-Earth Oxide Nanopolyhedra, Nanoplates, and Nanodisks. *Angew. Chem., Int. Ed.* **2005**, *44*, 3256–3260.
- (40) Zhou, Z.; Hu, R.; Wang, L.; Sun, C.; Fu, G.; Gao, J. Water Bridge Coordination on the Metal-Rich Facets of Gd_2O_3 Nanoplates Confers High T_1 Relaxivity. *Nanoscale* **2016**, *8*, 17887–17894.
- (41) Cao, Y. C. Synthesis of Square Gadolinium-Oxide Nanoplates. *J. Am. Chem. Soc.* **2004**, *126*, 7456–7457.
- (42) Paik, T.; Gordon, T. R.; Prantner, A. M.; Yun, H.; Murray, C. B. Designing Tripodal and Triangular Gadolinium Oxide Nanoplates

and Self-Assembled Nanofibrils as Potential Multimodal Bioimaging Probes. *ACS Nano* **2013**, *7*, 2850–2859.

(43) Suo, Z.; Ma, E. Y.; Gleskova, H.; Wagner, S. Mechanics of Rollable and Foldable Film-on-Foil Electronics. *Appl. Phys. Lett.* **1999**, *74*, 1177–1179.

(44) Grundmann, M. Nanoscroll Formation from Strained Layer Heterostructures. *Appl. Phys. Lett.* **2003**, *83*, 2444–2446.